

## CORRESPONDENCE OPEN



## Structural insights into ligand recognition and activation of human purinergic receptor P2Y14

© The Author(s) 2025

Cell Discovery; https://doi.org/10.1038/s41421-025-00799-9

Dear Editor,

Purinergic receptors, including P2Y1-like receptors (P2Y1, 2, 4, 6, and 11) that signal through  $G_{q/11}$  proteins and P2Y12-like receptors (P2Y12, 13, and 14) that activate  $G_{i/o}$  proteins, are involved in diverse physiological processes such as cell proliferation, chemotaxis, inflammation, cancer metastasis, cardiovascular events, neurodegenerative diseases, and aging. To date, active and inactive structures of P2Y1 and P2Y12 have been resolved, providing structural insights into P2Y receptor signaling mechanisms<sup>1</sup>. UDP-sugars, including UDP-glucose (UDPG), UDP-glucuronic acid (UDPGA), UDP-galactose, and UDP-*N*-acetylglucosamine, are produced in the cytoplasmic matrix under normal physiological conditions and play important roles in regulating blood sugar levels, fat metabolism, and inflammation<sup>2,3</sup>. UDP-sugars are secreted into the extracellular space to function as the paracrine signals through the G-protein-coupled purinergic receptor, P2Y14, which senses extracellular metabolic stress signals and regulates energy homeostasis<sup>4,5</sup>. P2Y14 couples to  $G_i$  signaling pathways, orchestrating a wide range of biological processes ranging from gastric function to immune responses, renal inflammation, and liver fibrosis<sup>6–8</sup>. Therefore, P2Y14 has emerged as a promising therapeutic target for asthma, acute kidney injury, and inflammatory bowel disease (IBD) (Fig. 1a)<sup>9–11</sup>. Despite its significance, the molecular activation mechanism underlying its ability to recognize diverse ligands and couple  $G_i$  protein remains elusive. There is an urgent need to delineate the molecular mechanism underlying P2Y14 signaling.

Endogenous UDP-sugars share common moieties, such as uridine and diphosphate groups, with their structural variations primarily arising from differences in the attached sugar groups. By comparing the structures of UDP-sugars with endogenous metabolites, we found that NADH exhibits characteristic chemical scaffolds, such as diphosphate and nicotinamide riboside, which are structurally similar to the uridine and diphosphate groups found in UDP sugars (Fig. 1b), suggesting that NADH may function as an endogenous agonist of P2Y14. To test our hypothesis, calcium-induced luciferase accumulation assays were performed to measure  $G_{q/11}$ -protein subtype activation in the presence of NADH. The results of the cellular assays showed that P2Y14 was activated by NADH in a dose-dependent manner, confirming that NADH functions as an endogenous agonist of P2Y14 (Fig. 1c).

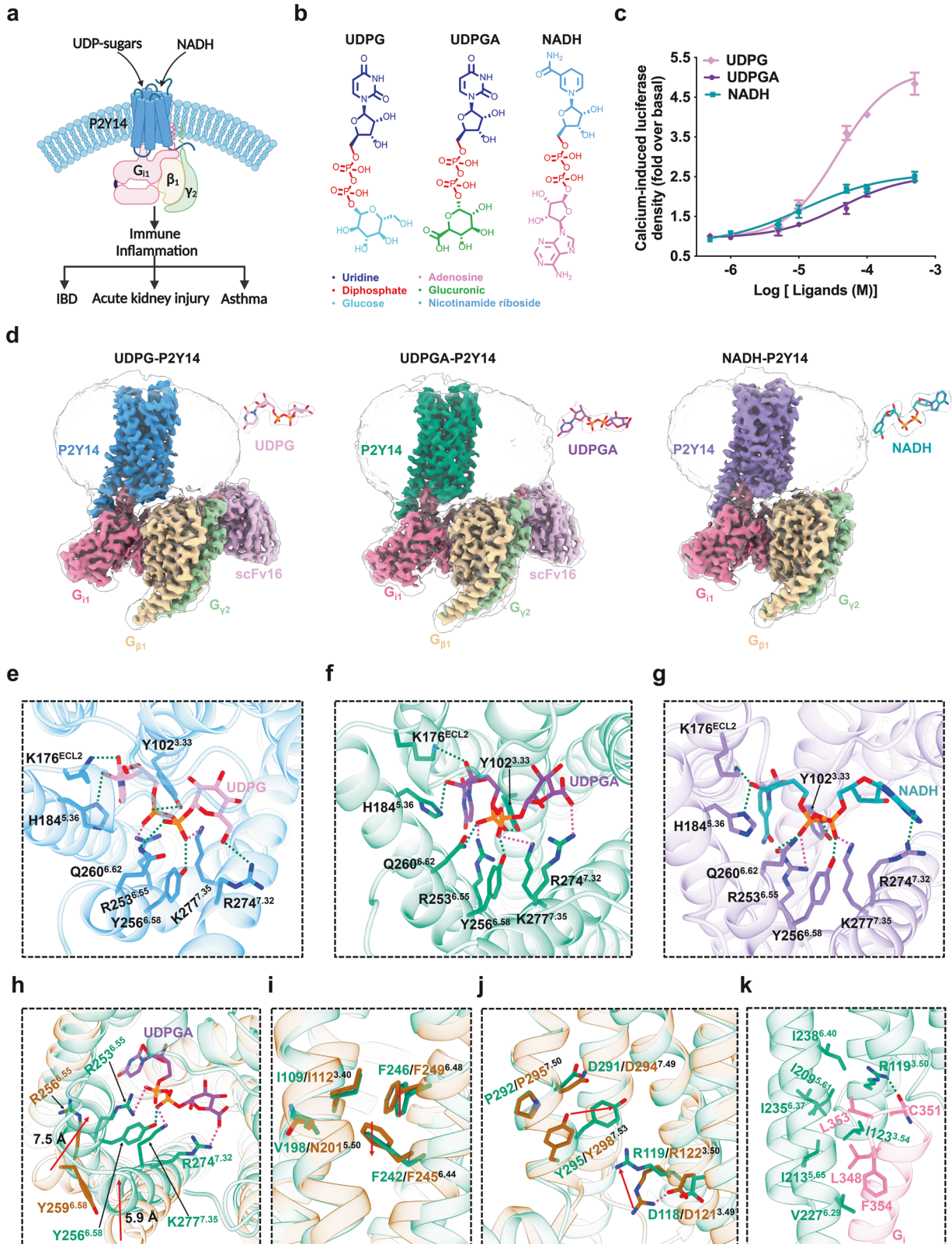
To investigate the molecular activation and  $G_i$  coupling mechanisms of P2Y14, we determined the cryo-electron microscopy (cryo-EM) structures of the  $G_i$  heterotrimer-coupled P2Y14 in complex with UDPG, UDPGA, and NADH, respectively. To obtain stable and homogeneous P2Y14- $G_i$  complexes, a BRIL tag was fused to the N-terminus of P2Y14, and a dominant-negative  $G_i$  was employed to facilitate complex assembly. The active-state structures of P2Y14 bound to the  $G_i$  heterotrimer and the

endogenous agonists were further stabilized using a single-chain antibody scFv16 (Supplementary Figs. S1a, b, S2a, b, S3a, b). Unexpectedly, the electron density for scFv16 was not observed in the map of the NADH-bound P2Y14- $G_i$  complex (Fig. 1d). The global resolutions of the  $G_i$ -coupled P2Y14 structures with UDPG, UDPGA, and NADH were determined to be 2.88 Å, 2.76 Å, and 2.76 Å, respectively (Supplementary Figs. S1c–h, S2c–h, S3c–h and Table S1). These structures exhibit a similar folding configuration, with the root mean square deviation (RMSD) values being less than 0.5 Å between the complexes (Supplementary Fig. S4a). The relatively high-quality density maps allowed accurate modeling of the seven-transmembrane (7TM) cores of the receptors, the  $G_i$  heterotrimer, and scFv16. In addition, the side chains of most residues are well-defined in all components, providing a precise modeling of the intermolecular interactions of P2Y14 with the agonists and  $G_i$  protein (Fig. 1d; Supplementary Figs. S1i, S2i, S3i).

Despite variations in agonist structures, the active-state orthosteric pockets in UDPG-, UDPGA-, and NADH-bound P2Y14 complexes share common features, consisting of residues in transmembrane helices TM2–TM7. The extracellular loop 2 (ECL2) acts as a “lip”, anchoring the agonists within the orthosteric pocket (Supplementary Fig. S4b). These agonists occupy an upper binding site in the receptor’s extracellular region, with the uridine groups in UDPG/UDPGA and the nicotinamide group in NADH penetrating deeply into a narrow cavity within the transmembrane core, where they form extensive interactions with TM4 and TM5. In contrast, the sugar groups of UDPG/UDPGA and the adenosine group of NADH face the extracellular surface, interacting with TM2 and TM7. Structural comparisons with other purinergic receptors, such as P2Y1 and P2Y12, reveal that the binding pockets of P2Y14 and P2Y12 extend deeper into the extracellular cavity than that of P2Y1 (Supplementary Fig. S4c). The NADH-binding pocket in P2Y14 is larger than those for UDPG and UDPGA, with volumes ranging from 443 Å<sup>3</sup> to 512 Å<sup>3</sup>, suggesting that the distinct geometry of NADH results in a larger binding pocket (Supplementary Fig. S4c). Due to the structural similarities among the agonists, the UDPG-, UDPGA-, and NADH-bound P2Y14 complexes share common ligand-interacting residues at the extracellular vestibule. These agonists primarily interact with the orthosteric pocket of P2Y14 through hydrogen-bonding and ionic interactions. The uridine groups of UDPG/UDPGA and the nicotinamide riboside group of NADH form hydrogen-bonding interactions with residues K176<sup>ECL2</sup> and H184<sup>5.36</sup> (superscripts indicate Ballesteros-Weinstein numbering for G-protein-coupled receptors (GPCRs)), along with  $\pi$ - $\pi$  stacking interactions with Y102<sup>3.33</sup> (Fig. 1e–g; Supplementary Fig. S5a–c). The diphosphate groups of these agonists are anchored through ionic interactions with residues R253<sup>6.55</sup> and K277<sup>7.35</sup>, as well as hydrogen-bonding interactions with Y102<sup>3.33</sup>, Y256<sup>6.58</sup>, and Q260<sup>6.62</sup> (Fig. 1e–g; Supplementary Fig. S5a–c). Additionally, the residue R274<sup>7.32</sup> forms hydrogen-bonding and ionic interactions with the sugar groups of UDPG/UDPGA and the adenosine group of NADH (Fig.

Received: 22 October 2024 Accepted: 31 March 2025

Published online: 13 May 2025



1e–g; Supplementary Fig. S5a–c). In functional assays, mutations of these interacting residues resulted in a decreased agonist potency for UDPG, UDPGA, and NADH (Supplementary Fig. S5d–h and Table S2). Beyond these common interactions, other residues in P2Y14 engage in specific polar and hydrophobic interactions

with the agonists, creating distinct interaction patterns. For example, UDPG interacts with D81<sup>2.64</sup> and N156<sup>4.60</sup>; UDPGA with K77<sup>2.60</sup>, N90<sup>3.21</sup>, N156<sup>4.60</sup>, and N188<sup>5.40</sup>; and NADH with K77<sup>2.60</sup>, Y106<sup>3.37</sup>, N188<sup>5.40</sup>, F191<sup>5.43</sup>, and E278<sup>7.36</sup> (Supplementary Fig. S5a–c, i). The subtle structural differences between UDPG and

**Fig. 1 Structure basis of P2Y14 activation.** **a** Schematic representation of P2Y14-mediated activation of downstream  $G_i$  protein signaling pathways in response to various ligands. **b** Chemical structures of the endogenous agonists used in this study. The chemical groups of endogenous agonists were represented in distinct colors. **c** Agonist potency on G-protein signaling in P2Y14, analyzed using a calcium-induced luciferase accumulation assay. Data are shown as the mean  $\pm$  SEM, from three independent measurements. **d** Cryo-EM density maps of the UDPG-, UDPGA-, and NADH-bound P2Y14- $G_i$  complexes. **e–g** Interactions between UDPG (pink) with P2Y14 (blue) (**e**), UDPGA (violet) with P2Y14 (strong cyan) (**f**), and NADH (cyan) with P2Y14 (purple) (**g**). **h** Structural comparison between the active P2Y14 (strong cyan) and inactive P2Y12 (dark orange). **i** Structural rearrangement of the PIF triad and toggle switch during P2Y14 activation. **j** Structural rearrangement of the E/DRY and NPXXY motifs during P2Y14 activation. **k** Detailed interactions of P2Y14 with the  $\alpha 5$ -helix of  $G_i$  in the UDPGA-bound P2Y14 structure. Hydrogen-bonding interactions are shown with green dashed lines, and ionic interactions are shown with pink dashed lines.

UDPGA arise from their sugar groups, which contribute to distinct agonist recognition patterns. The residues D81<sup>2,64</sup> and N90<sup>3,21</sup> establish hydrogen-bonding interactions with UDPG and UDPGA, respectively. In functional assays, the D81<sup>2,64</sup>A mutation led to a more substantial decrease in UDPG activity compared to that in UDPGA. Conversely, the N90<sup>3,21</sup>A mutation caused a more significant reduction in UDPGA activity than in UDPG (Supplementary Fig. S5a, b, g). Additionally, NADH exhibits unique ligand-receptor interactions by forming hydrogen bonds with residues Y106<sup>3,37</sup> and E278<sup>7,36</sup>. Y106<sup>3,37</sup>A and E278<sup>7,36</sup>A mutants of P2Y14 showed significantly reduced activation by NADH relative to UDPG and UDPGA (Supplementary Fig. S5a–g). Notably, previous study reported that K77<sup>2,60</sup> is crucial for the recognition of the sugar groups in UDP-sugars<sup>12</sup>. However, in the UDPG-bound P2Y14 structure, K77<sup>2,60</sup> is distant from the UDP-sugars and instead forms a salt bridge with E278<sup>7,36</sup>, stabilizing the architecture of the orthosteric cavity (Supplementary Fig. S6a). The mutation at K77<sup>2,60</sup> resulted in a larger decrease in the activity of UDPG compared to the mutation at E278<sup>7,36</sup>, which can be attributed to the significantly higher structural instability observed in the K77<sup>2,60</sup>A mutant (Supplementary Fig. S6b, c). To further validate the agonist-binding poses, we performed all-atom molecular dynamics (MD) simulations (400 ns) on these P2Y14 systems. RMSD results showed that UDPG, UDPGA, and NADH remained close to their initially modeled poses throughout the simulations (Supplementary Fig. S7).

P2Y14 belongs to the  $\delta$ -branch GPCR subfamily, including SUCR1, P2Y1, P2Y12, HCA2, CysLT1/2, PAR1/2, PAFR, GPR35, and LPA6. The lack of an inactive P2Y14 structure has hindered the understanding of its activation mechanism. The closest phylogenetic neighbor of P2Y14 is P2Y12 receptor that also couples to  $G_i$  protein. Therefore, the determined structure of the AZD1283-bound inactive P2Y12 complex (PDB: 4NTJ) allowed us to infer the activation mechanism of P2Y14. A comparison of the UDPGA-bound active P2Y14 with the AZD1283-bound inactive P2Y12 revealed distinct conformations on both the extracellular and intracellular sides. In the P2Y14 structure, UDPGA binding causes inward movements of the extracellular region of TM6 for  $\sim 7.5$  Å (relative to the  $\alpha$ -carbon distance between K258<sup>6,60</sup> in P2Y14 and L261<sup>6,60</sup> in P2Y12) and that of TM7 for  $\sim 5.9$  Å (relative to the  $\alpha$ -carbon distance between S266<sup>7,24</sup> in P2Y14 and D269<sup>7,24</sup> in P2Y12), along with an outward shift in TM6's intracellular portion for  $\sim 7.8$  Å (relative to the  $\alpha$ -carbon distance between K228<sup>6,30</sup> in P2Y14 and R231<sup>6,30</sup> in P2Y12) compared to P2Y12 (Fig. 1h; Supplementary Fig. S8a, b). The agonist-induced upward shift of TM3 is a key activation feature in  $\delta$ -branch receptors like P2Y1, P2Y12, HCA2, and SUCR1<sup>13</sup>, driven by interactions with a positively charged residue in TM3. However, this shift is absent in active P2Y14, suggesting that P2Y14 activation is independent of TM3's conformational rearrangement. Additionally, P2Y14 lacks the characteristic proline kink (P<sup>5,50</sup>) found in most class A GPCRs, where it typically induces a bend in TM5 during transducer coupling. Instead, P2Y14 has V198<sup>5,50</sup>, which results in a straight TM5, similar to P2Y12 and HCA2 (Supplementary Fig. S8c–e). Moreover, the conserved toggle switch residue in the majority of class A GPCR is W<sup>6,48</sup>. However, the toggle switch at position 6.48




is occupied by a less bulky residue (F/Y/L<sup>6,48</sup>) in  $\delta$ -branch GPCRs, leading to a toggle switch movement rather than the typical W<sup>6,48</sup> rotation during activation. In the inactive P2Y12 structure, the side chains of the residues R256<sup>6,55</sup> and Y259<sup>6,58</sup> in TM6 are positioned away from the orthosteric pocket (Fig. 1h). Upon UDPGA binding to P2Y14, the side chains of R253<sup>6,55</sup> and Y256<sup>6,58</sup> rotate towards the orthosteric pocket, forming polar interactions with UDPGA and triggering downward shifts of toggle switch F246<sup>6,48</sup> and F242<sup>6,44</sup> of the PIF triad (V198<sup>5,50</sup>/I109<sup>3,40</sup>/F242<sup>6,44</sup>) (Fig. 1i). Additionally, UDPGA binding also establishes hydrogen-bonding interactions with the residues R274<sup>7,32</sup> and K277<sup>7,35</sup> in TM7, inducing inward movement of TM7's extracellular region. Subsequently, conformational rearrangements of the conserved E/DR<sup>3,50</sup>Y and N<sup>7,49</sup>P<sup>7,50</sup>XXY<sup>7,53</sup> motifs (DR119<sup>3,50</sup>Y and D291<sup>7,49</sup>PVIFY in P2Y14) are triggered simultaneously. In the UDPGA-bound P2Y14 structure, the side chain of R119<sup>3,50</sup> extends toward TM7 and packs closely with the D291<sup>7,49</sup>PVIFY motif compared to the inactive P2Y12 structure (Fig. 1i, j), allowing for the insertion of the C-terminus of the  $G_i$  protein. Together, these findings indicate that P2Y14 activation involves a cascade of conformational changes, particularly in TM6 and TM7, transmitting the activation signal from the extracellular region to the intracellular portion.

The structural determination of the P2Y14- $G_i$  complexes offers valuable insights for dissecting the  $G_i$  coupling mechanism. Given the higher resolution of the UDPGA-bound P2Y14 structure, it was selected for detailed analysis of the receptor- $G_i$  protein interactions. Structural comparisons of UDPGA-bound P2Y14- $G_i$  with other  $G_i$ -coupled GPCR structures revealed that the  $\alpha 5$ -helix of  $G_i$  in P2Y14- $G_i$  closely resembles that of GPR84- $G_i$  in terms of orientation and movements (Supplementary Fig. S9). In the active P2Y14 complex, the interactions between  $G_i$  and the cytoplasmic cavity of P2Y14 are primarily contributed by TM3, TM5, and TM6 of the receptors (Fig. 1k). The  $\alpha 5$  helix of  $G_i$  is amphipathic and forms extensive hydrophobic and hydrogen-bonding interactions with the cytoplasmic cavity of P2Y14. The residue R119<sup>3,50</sup> of the DRY motif establishes hydrogen-bonding interaction with the  $\alpha 5$ -helix backbone of  $G_i$  protein, playing a key role in G-protein activation. Mutation of this residue in P2Y14 reduced  $G_i$  protein signaling (Supplementary Fig. S10a–c). Additionally, the side chains of F354, F353, C351, and L348 in the  $\alpha 5$ -helix of  $G_i$  are involved in extensive hydrophobic interactions with the hydrophobic pocket (I123<sup>3,54</sup>, I209<sup>5,61</sup>, I213<sup>5,65</sup>, V227<sup>6,29</sup>, I235<sup>6,37</sup>, and I238<sup>6,40</sup>) in P2Y14 (Fig. 1k). These hydrophobic interactions of P2Y14 with  $G_i$ 's  $\alpha 5$ -helix were further confirmed by the functional assays (Supplementary Fig. S10a–c).

P2Y14 is widely distributed in placenta, spleen, bone marrow, thymus, stomach, intestine, adipose tissue, lung, and brain, and has recently attracted attention as a potential drug target for asthma, acute kidney injury, and IBD. The determination of experimental P2Y14 structure is critical for understanding its pathophysiological roles and facilitating drug design. The cryo-EM structures obtained in this study elucidate the agonist recognition mechanism of P2Y14, which primarily depends on polar interactions between the agonist and the receptor. These distinct polar interaction networks within P2Y14's orthosteric pocket offer new avenues for designing synthetic ligands with diverse structures. While agonist-induced rearrangement of TM3 is a common



activation mechanism among  $\delta$ -branch GPCRs, P2Y<sub>14</sub> exhibits an atypical activation mode, driven by agonist-induced conformational changes in TM6 and TM7. NADH, a key factor in transferring electrons from the tricarboxylic acid cycle to the electron transport chain, plays a central role in energy metabolism and ATP production<sup>14</sup>. While earlier studies have primarily focused on NADH's intracellular functions, recent research suggests that NADH may also act as a paracrine signal<sup>15</sup>. However, the molecular recognition mechanism by which extracellular NADH mediates signal transduction through membrane receptors remains unclear. Our study is the first to identify NADH as an endogenous agonist of P2Y<sub>14</sub>, supported by cellular functional assays and the active cryo-EM structure of the NADH-bound P2Y<sub>14</sub>-G<sub>i</sub> complex, revealing the NADH molecular recognition mechanism. This suggests that NADH functions as a paracrine signal through P2Y<sub>14</sub>, playing crucial roles in immune and inflammatory responses. In conclusion, our findings provide important insights into receptor-ligand interactions and downstream transducer coupling mechanisms in P2Y<sub>14</sub>, offering a foundation for structure-based drug design.

Quanchang Gu<sup>1,2,3,6</sup>, Zhenyu Lv<sup>2,6</sup>, Tianxin Wang<sup>1,2,3,4,5,6</sup>  
Wenqin Tang<sup>2,3,6</sup>, Xuzhen Guo<sup>1</sup>, Xiangling Huang<sup>2</sup>, Fahui Li<sup>2,3,4,5,6</sup>  
and Jiangyun Wang<sup>1,2,3,4,5,6</sup>

<sup>1</sup>CAS Key Laboratory of Quantitative Engineering Biology, Institute of Synthetic Biology, Shenzhen Institute of Advanced Technology, Chinese Academy of Sciences, Shenzhen, Guangdong, China. <sup>2</sup>Key Laboratory of Biomacromolecules (CAS), CAS Center for Excellence in Biomacromolecules, Institute of Biophysics, Chinese Academy of Sciences, Beijing, China. <sup>3</sup>School of Life Sciences, University of Chinese Academy of Sciences, Beijing, China. <sup>4</sup>iHuman Institute, ShanghaiTech University, Shanghai, China. <sup>5</sup>School of Life Science and Technology, ShanghaiTech University, Shanghai, China. <sup>6</sup>These authors contributed equally: Quanchang Gu, Zhenyu Lv, Tianxin Wang, Wenqin Tang. ✉email: lifahui@moon.ibp.ac.cn; jwang@ibp.ac.cn

## ACKNOWLEDGEMENTS

We acknowledge support from the National Key R&D Program of China (2020YFA0907701, 2024YFA0917503, 2023YFA0916300, 2021YFA0910202, and 2022YFA1304701), the National Natural Science Foundation of China (22121003, 22107113, 32071299, and 32027901), the Strategic Priority Research Program of Chinese Academy of Sciences (XDB37040203), and the CAS Project for Young Scientists in Basic Research (YSBR-015 and YSBR-072-6). We thank Junlin Liu, Suwen Hu, and Na Chen from Insect Cell Expression Core, and Xiaoyan Liu and Pei Si from Mammalian Cell Expression Core for biomass production. The cryo-EM data were collected at the Bio-Electron Microscopy Facility of ShanghaiTech University with the assistance of Li Wang, Dandan Liu, Qianqian Sun, and Xiaoli Guo. We also thank Qiaoyun Shi from the Protein Purification Core, and Lu Zhang, Qiwen Tan, and Fangfang Zhou from the Cloning and Assays Cores of iHuman Institute for technical support.

## AUTHOR CONTRIBUTIONS

J.W. organized the project. F.L., Q.G., and W.T. guided all the structural analyses. F.L. and Q.G. designed all the mutants for functional analysis. Q.G., T.W., and X.H. developed the P2Y<sub>14</sub> constructs and optimized protein expression. Q.G. and T.W. performed protein expression, prepared samples for cryo-EM grids, and collected the

cryo-EM data. W.T. performed cryo-EM map calculation, model building, structure refinement, and MD simulations. Z.L., Q.G., and X.G. performed functional assays. F.L. and J.W. wrote the manuscript. All the authors have read and commented on the manuscript.

## DATA AVAILABILITY

The cryo-EM density maps have been deposited in the Electron Microscopy Data Bank (EMDB) and Protein Data Bank (PDB) under accession numbers EMD-61052, EMD-63224 (composite) and 9J0B for UDPG-P2Y<sub>14</sub>-G<sub>i</sub> complex; EMD-61055 and 9J0I for UDPGA-P2Y<sub>14</sub>-G<sub>i</sub> complex; EMD-61054, EMD-63223 (composite) and 9J0F for NADH-P2Y<sub>14</sub>-G<sub>i</sub> complex.

## CONFLICT OF INTEREST

The authors declare no competing interests.

## ADDITIONAL INFORMATION

**Supplementary information** The online version contains supplementary material available at <https://doi.org/10.1038/s41421-025-00799-9>.

**Correspondence** and requests for materials should be addressed to Fahui Li or Jiangyun Wang.

**Publisher's note** Springer Nature remains neutral with regard to jurisdictional claims in published maps and institutional affiliations.

## REFERENCES

- Li, B. et al. *Protein Cell* **14**, 382–386 (2023).
- Jain, S. et al. *JCI Insight* **6**, e146577 (2021).
- Ma, J. et al. *Nat. Commun.* **11**, 1769 (2020).
- Lazarowski, E. R. & Harden, T. K. *Mol. Pharm.* **88**, 151–160 (2015).
- Garrison, B. S. & Rossi, D. J. *J. Clin. Invest.* **124**, 2846–2848 (2014).
- Foster, P. S., Tay, H. L. & Hogan, S. P. *J. Clin. Invest.* **131**, e147735 (2021).
- Battistone, M. A. et al. *J. Clin. Invest.* **130**, 3734–3749 (2020).
- Mederacke, I. et al. *Sci. Transl. Med.* **14**, eabe5795 (2022).
- Karcz, T. P. et al. *J. Clin. Invest.* **131**, e140709 (2021).
- Breton, S. & Brown, D. *Ann. Nutr. Metab.* **72**, 11–16 (2018).
- Wang, Y. H. et al. *J. Med. Chem.* **67**, 11989–12011 (2024).
- Zhao, L. et al. *Elife* **12**, e85449 (2023).
- Suzuki, S. et al. *Nat. Commun.* **14**, 5899 (2023).
- Verdin, E. *Science* **350**, 1208–1213 (2015).
- Flieger, R. et al. *Biochem. Soc. Trans.* **47**, 329–337 (2019).



**Open Access** This article is licensed under a Creative Commons Attribution 4.0 International License, which permits use, sharing, adaptation, distribution and reproduction in any medium or format, as long as you give appropriate credit to the original author(s) and the source, provide a link to the Creative Commons licence, and indicate if changes were made. The images or other third party material in this article are included in the article's Creative Commons licence, unless indicated otherwise in a credit line to the material. If material is not included in the article's Creative Commons licence and your intended use is not permitted by statutory regulation or exceeds the permitted use, you will need to obtain permission directly from the copyright holder. To view a copy of this licence, visit <http://creativecommons.org/licenses/by/4.0/>.

© The Author(s) 2025